Diagnosing model error in canopy-atmosphere exchange using empirical orthogonal function analysis

Darren T. Drewry[1] and John D. Albertson[1,2]

Received 11 August 2005; revised 21 January 2006; accepted 2 March 2006; published 27 June 2006.

[1] The application of complex land surface models to long-term estimation of water, energy, and CO_2 exchange suffers from possible static parameterization of inherently time-varying properties. This paper presents a method by which structural (i.e., spatial) patterns in model output errors can be identified and associated with errors in a single parameter or set of interacting parameters. We focus on CO_2 concentration profiles as the observed quantity containing spatial information on model performance. The core of the method relies on the empirical orthogonal function (EOF) analysis of an ensemble of model error profiles produced by synthetically inducing parameter biases. EOF analyses of the error profiles associated with photosynthetic capacity, stomatal conductance, radiation interception, soil respiration, and turbulent mixing parameters concentrated greater than 94% of the error pattern variability in the first two EOFs, producing very compact (two member) basis sets. Application of the EOFs to the identification of parameter error sources was performed with three sets of synthetic tests. The method was broadly successful at identifying the primary error source when one or two error sources were present, using single-parameter basis sets. Two-parameter basis sets were able to identify strongly interacting parameter errors (i.e., errors of approximately equal magnitude). Environmental classification of photosynthetically active radiation and wind speed regimes was effective at untangling error influences for the tightly coupled photosynthetic, radiation, and stomatal conductance parameters. Data analysis of measured concentration profiles was used to derive the environmental classes.

Citation: Drewry, D. T., and J. D. Albertson (2006), Diagnosing model error in canopy-atmosphere exchange using empirical orthogonal function analysis, *Water Resour. Res.*, *42*, W06421, doi:10.1029/2005WR004496.

1. Introduction

[2] Estimation of the exchange of water vapor, energy and carbon dioxide (CO_2) between the land surface and the overlying atmosphere has become a major focus for researchers attempting to quantify the impact of forest ecosystems on the global water and carbon budgets. Recently, with long-term eddy covariance flux records becoming available, examination of the seasonal-to-annual variability of the processes driving land-atmosphere exchange, at scales ranging from a single, homogeneous stand to more extensive and heterogeneous sites, has received increasing attention. Several factors have been identified as causes of net ecosystem exchange (NEE) variation over timescales of one month or more. These include drought induced water stress [*Baldocchi*, 1997; *Ellsworth*, 2000; *Wilson et al.*, 2000a; *Hollinger et al.*, 2004], leaf age and physiological change [*Sullivan et al.*, 1997; *Chen et al.*, 1999; *Ellsworth*, 2000; *Wilson et al.*, 2000a], acclimation to light [*Middleton et al.*, 1997; *Morecroft and Roberts*, 1999] and environmental conditions [*Greco and Baldocchi*, 1996; *Baldocchi et al.*, 1997; *Chen et al.*, 1999; *Lloyd et al.*, 2002; *Hollinger et al.*, 2004], and changes in ambient CO_2 concentration [*Ellsworth*, 1999] and soil temperature [*Middleton et al.*, 1997].

[3] With the increasing need for accurate, long-term estimation of canopy-atmosphere exchange, the challenge presented by the temporal variability of vegetation functioning has driven the growth in mechanistic detail and complexity of models designed to estimate land-atmosphere fluxes of CO_2, water vapor and energy. One modeling framework that has been broadly used as a tool for hypothesis testing and flux estimation is based on the vertical discretization of a plant canopy into multiple layers. This framework, referred to here as a multilayer canopy process model (MLCPM), consists of a set of coupled component submodels representing the physical and biological processes governing mass and energy exchanges across the canopy-atmosphere interface. Models of this type have proven relatively accurate with respect to net (i.e., vertically integrated) flux estimation across a broad range of ecosystems [e.g., *Baldocchi and Harley*, 1995; *Leuning et al.*, 1995; *Gu et al.*, 1999; *Lai et al.*, 2000b; *Pyles et al.*, 2000; *Styles et al.*, 2002]. Despite their broad applicability, unique parameterizations are required in each case [*Wullschleger*, 1993]. Most often these parameters are treated as static values, despite being known to vary seasonally and interannually, as canopy structure [*Pinard and Wilson*, 2001; *Baldocchi et al.*, 2002], leaf age [*Wilson et al.*, 2000a, 2001], and

[1]Department of Civil and Environmental Engineering, Duke University, Durham, North Carolina, USA.
[2]Nicholas School of the Environment and Earth Sciences, Duke University, Durham, North Carolina, USA.

0043-1397/06/2005WR004496

environmental conditions vary [*Ellsworth*, 2000; *Law et al.*, 2000; *Wilson et al.*, 2000b; *Cai and Dang*, 2002; *Medlyn et al.*, 2002; *Xu and Baldocchi*, 2003]. This limits the applicability of MLCPMs to short-term integrations with similar environmental conditions to those for which the submodel parameters were measured.

[4] Recently, methodologies have been presented to optimize static parameter values through the minimization of residuals between modeled fluxes and concentrations and those measured within and above plant canopies. *Styles et al.* [2002] optimized nine MLCPM parameter values against measured scalar concentrations, and concluded the model could not significantly distinguish the parameter influences, resulting in potential interdependencies among the optimized values. Using the CSIRO biospheric model and measured fluxes of CO_2, water vapor and heat in a nonlinear inversion framework, *Wang et al.* [2001] found that a maximum of three or four parameters could be independently resolved. Strong correlation between parameters, similar effects of parameter perturbations on model outputs, and model insensitivity to specific parameters were all reasons for the limitation.

[5] *Franks et al.* [1997] note that multiple sets of parameters may achieve an optimization goal equally well in a complex land-atmosphere scheme (i.e., the equifinality problem). Monte Carlo–based methods have been developed to deal with equifinality by estimating the uncertainty of models and parameter sets, notably the GLUE methodology of *Beven and Freer* [2001] and the Metropolis algorithm of *Kuczera and Parent* [1998]. Multiobjective optimization has also been applied successfully to deal with uncertainty in large parameter spaces [e.g., *Gupta et al.*, 1999; *Mackay et al.*, 2003]. However, to our knowledge, no attempt has been made to examine spatial error structures in the predictions associated with specific model errors as a way to select the most likely sources of error for use in an optimization scheme.

[6] This paper presents a method by which structural (i.e., spatial) patterns in model output errors can be identified and associated with errors in a single, or set of interacting, parameters. The core of the method relies on the empirical orthogonal function (EOF) analysis of model error structures produced by synthetically inducing specific parameter biases. EOF analysis produces an orthogonal decomposition of a spatial covariance matrix, in this case model error covariances, information critical to the success of modern data assimilation systems, [e.g., *Reichle et al.*, 2001; *Margulis and Entekhabi*, 2003]. The orthogonal nature of the EOF patterns allows them to naturally form basis sets onto which model/data residuals may be projected. The method is applied to the identification of the primary source(s) of parameter error in modeled canopy sublayer CO_2 concentration profiles through a set of synthetic experiments in which single and multiple error source cases are considered. Concentration profiles are a data source primarily collected to calculate mass storage (e.g. CO_2) within the canopy airspace [*Hollinger et al.*, 1994; *Baldocchi et al.*, 1996; *Lai et al.*, 2000a]. We propose here the use of residual concentration profiles as a vertical gauge of MLCPM fidelity.

[7] Successful MLCPM validations for short time periods, and studies demonstrating the divergence of modeled and measured fluxes at longer timescales, point to model bias caused by parameter error as a major concern [*Baldocchi and Wilson*, 2001; *Katul et al.*, 2001]. In this preliminary study, potential error sources are limited to parameter values, omitting consideration of measurement error and model structural error. We also address the potential for conditioning the analysis on background environmental conditions (e.g. photosynthetically active radiation and wind speed) as a means to separate the effects of different error sources.

2. Theory

2.1. Empirical Orthogonal Function (EOF) Analysis

2.1.1. General Overview and Example Application

[8] EOF analysis, also known as Principal Component analysis, owes its origins to *Pearson* [1901] and *Hotelling* [1933]. The technique was originally introduced into meteorology [*Lorenz*, 1956] as a method for extracting the dominant modes of spatial variability in meteorological fields. The spatial patterns optimally describe the variance of the original data set [*von Storch and Zwiers*, 1999], such that, in many cases, a large fraction of the degrees of freedom of the original data set can be eliminated as unimportant, while retaining the majority of the information contained in the original data set.

[9] We examine the properties of EOF analysis by considering an application to a set of measured CO_2 concentration profiles collected at 0.75, 1.5, 3.5, 5.5, 7.5, 9.5, 11.5, 13.5, and 15.5 m above the soil surface in the Duke Forest Loblolly pine stand between the months of April and October in 2000. Details concerning the data collection methodology are given by *Lai et al.* [2000a, 2000b] and *Siqueira et al.* [2000]. Leaf area density profiles (L) defined the canopy height to be 16 meters.

[10] An r-by-n data matrix, $\mathbf{D}$, is constructed such that the n columns are each a measured concentration profile with r spatial coordinates (z) collected at unique, but not necessarily consecutive, measurement times. The profiles are centered by removal of the temporal mean vector. For the cases considered in this paper, there will always be many more data vectors than spatial coordinates (i.e., $r \ll n$). Application of EOF analysis expands $\mathbf{D}$ into a set of r orthogonal patterns, the EOFs (ϕ), and corresponding amplitude vectors, the principal components or PCs (ω), of length n. Figures 1a–1c present the first three EOFs of the daytime ($Q > 10$ μmol m^{-2} s^{-1}, 2879 records), nighttime (2295 records) and the combined (5174 records) sets of measured concentration profiles. The corresponding PCs are displayed in Figure 2, plotted against the hour of day and simultaneous measurements of photosynthetically active radiation (Q) and wind speed (U). These PC values are used to partition Q and U into environmental classes in the synthetic experiments that follow. The full set of EOFs span the vectors in the data matrix, allowing for the complete reconstruction of any data vector. A data vector corresponding to time t, $\mathbf{d}_t$, is equivalent to a linear combination of the EOFs, weighted by the amplitudes for t.

$$\mathbf{d}_t = \sum_{k=1}^{r} \omega_k(t)\phi_k \tag{1}$$

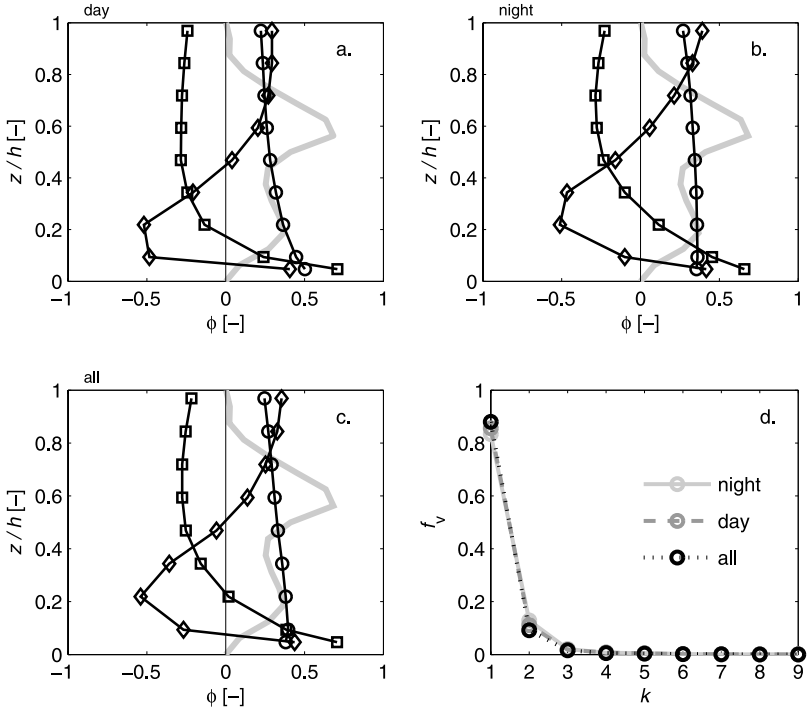

Figure 1. First three EOFs produced in the analysis of CO_2 profile data collected at the Duke Forest pine site, for (a) daytime, (b) nighttime, and (c) combined profile sets and (d) the fraction of data set variance described by each EOF. EOFs 1, 2, and 3 are plotted with circles, squares, and diamonds, respectively. L is plotted for reference as a thick gray line.

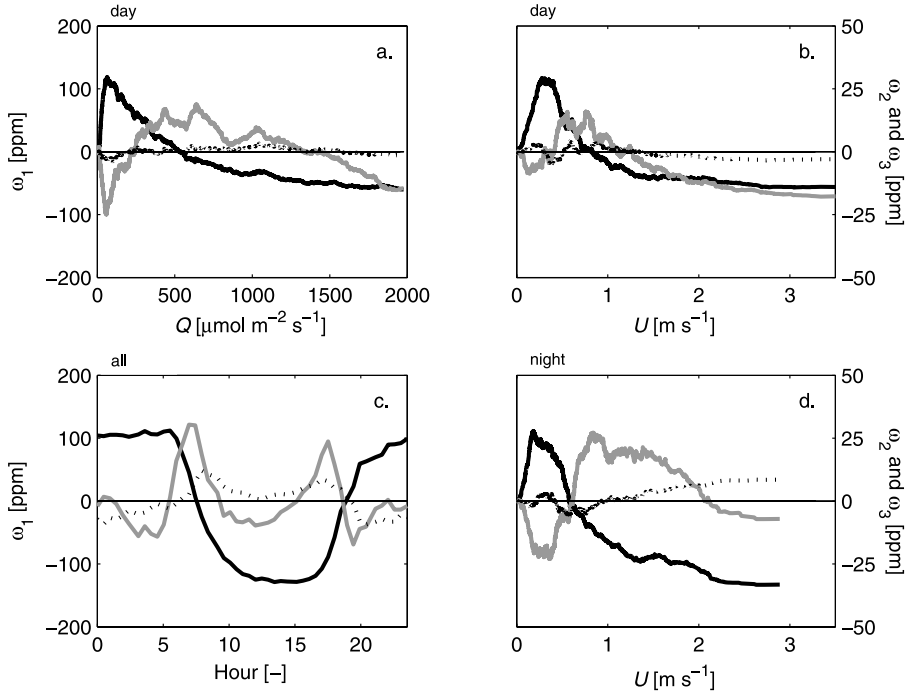

Figure 2. PCs 1–3 for daytime data plotted against (a) Q and (b) U. (c) Average PC values versus hour of day for the entire data set (daytime and nighttime data). (d) PCs 1–3 versus U for nighttime data. PCs in Figures 2a, 2b, and 2d are displayed as 200-point moving averages. The left-side ordinate corresponds to PC 1, and the right-side ordinate corresponds to PCs 2 and 3. Lines show ω_1 (solid black line), ω_2 (solid gray line), and ω_3 (dashed black line).

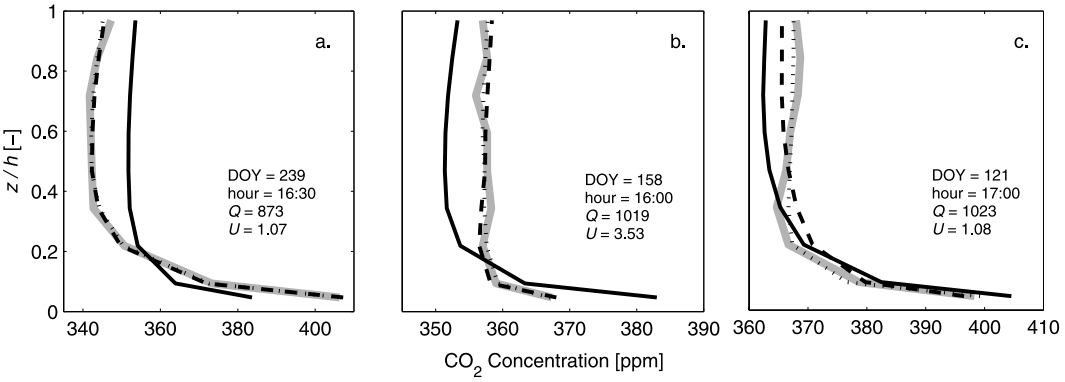

Figure 3. Reconstructions of three measured CO_2 concentration profiles using the first one (solid black line), two (dashed black line), and three (dotted black line) daytime EOFs. The measured profiles are displayed as thick gray lines. The day of year and time of each profile measurement are labeled on the subplot as well as the measured photosynthetically active radiation (Q) and wind speed (U) (in [μmol m^{-2} s^{-1}] and [m s^{-1}], respectively).

Three concentration profile reconstructions, using the EOFs in Figure 1a, are presented in Figure 3.

[11] The EOFs can be shown to be the eigenvectors of the sample spatial covariance matrix of **D** [*von Storch and Zwiers*, 1999]. The jth eigenvalue, λ_j, is the variance of the data set described by ϕ_j [*von Storch*, 1999]. The fraction of the variance (f_v) that can be attributed to ϕ_j is calculated as

$$f_v(j) = \lambda_j \Big/ \sum_{k=1}^{r} \lambda_k . \tag{2}$$

Plots of f_v in Figure 1d display a rapid decrease in variability described by each EOF, with the first EOF containing approximately 88% of data set variability, and the first three EOFs describing almost all of the profile variation. The amplitude vector of the kth EOF, ω_k, is calculated as

$$\omega_k = \phi_k^T \mathbf{D}. \tag{3}$$

The optimality of EOF analysis concentrates data variance in the first few spatial patterns. This allows the truncation of the series in (1), keeping only the first few significant patterns, while effectively capturing the majority of the signal in the data set.

2.1.2. Multilayer Canopy Process Model Formulation

[12] The focus of this study is to demonstrate the effects of parameter perturbations on the vertical geometry of model solutions, and to use the unique spatial structures associated with errors in each parameter, or set of parameters, to deduce the primary source of model error. An MLCPM capable of producing a solution of the vertically resolved radiation, wind speed, air temperature, scalar concentration and scalar source/sink strength profiles within the canopy was used to produce the error patterns and test the method described below. Model inputs include meteorological forcing at the canopy top, a leaf area density profile, and canopy-specific component submodel parameter values. While variation in component submodel formulations exist, a large number of studies have demonstrated the ability of MLCPMs to capture reasonably well the half-hour variability in canopy top fluxes when rigorous parameterization is performed under conditions similar to those for which the model is applied [*Baldocchi and Harley*, 1995; *Leuning et al.*, 1995; *Williams et al.*, 1996; *Gu et al.*, 1999; *Lai et al.*, 2000b; *Styles et al.*, 2002; *Ogee et al.*, 2003]. In the present study the MLCPM structure was kept simple and general, and is based primarily on that used previously to model the Duke Forest loblolly pine canopy [*Lai et al.*, 2000a, 2000b]. For brevity, we refer the reader to these studies for details regarding the model formulation and parameterization. Only those equations related to the parameters being investigated, or deviations in formulation from these studies, are presented here.

[13] A brief description of the component submodel formulations critical to the error determination methodology follows. The wind speed profile is computed using the steady state and horizontally homogeneous mean momentum equation,

$$-K_M \frac{d^2U}{dz^2} - \frac{dK_M}{dz}\frac{dU}{dz} + \frac{1}{2} C_d L U|U| = 0, \tag{4}$$

with a K theory closure for the Reynolds stress and a closure for the aerodynamic force dependent on the drag coefficient (C_d) and L [*Poggi et al.*, 2004]. Turbulent scalar transport is similarly computed using the temporally averaged conservation of mass equation, assuming negligible scalar storage [*Poggi et al.*, 2004]. The eddy diffusivity (K_M) is computed using the K theory closure

$$K_M = l_{mix}^2 \left| \frac{dU}{dz} \right|, \tag{5}$$

with a simple mixing length (l_{mix}) model,

$$l_{mix} = \begin{cases} \alpha \cdot h & (z < d) \\ \alpha \cdot h + 0.4 \cdot (z - d) & (z \geq d) \end{cases}, \tag{6}$$

and d being the zero-plane displacement height [*Katul et al.*, 2004; *Poggi et al.*, 2004]. The parameter α is static and determined by calibration.

[14] The radiation submodel algorithms compute separately the vertical interception of both direct beam and diffuse radiation in short- and long-wave bands [*Campbell and Norman*, 1998]. The extinction coefficient for beam radiation (K_b),

$$K_b(\psi) = \beta \cdot \frac{\sqrt{y^2 + \tan^2(\psi)}}{y + 1.774 \cdot (y + 1.182)^{-0.733}}, \quad (7)$$

depends on solar zenith angle (ψ) and the geometry of the leaf angle distribution (y). A multiplicative factor (β) is used in this equation as a parameter value that may induce error into the radiation submodel.

[15] The model of photosynthetic CO_2 uptake [*Farquhar et al.*, 1980; *Collatz et al.*, 1991] considers the biochemical limitations associated with electron transport (A_j) and Rubisco activity (A_c),

$$A_c = \frac{V(c_i - \Gamma_*)}{c_i + K_c(1 + [O_2]/K_{o2})}, \quad (8)$$

where Γ_* is the light compensation point for CO_2 assimilation, K_c and K_{o2} are Michaelis constants for the fixation of CO_2 and oxygen inhibition, respectively, $[O_2]$ is the ambient oxygen concentration, and V is a parameter representing Rubisco activity at 25°C.

[16] A linear relationship between stomatal conductance (g_s) and the product of photosynthetic uptake (A_n), relative humidity at the leaf surface (h_s) and CO_2 concentration at the leaf surface (C_s), couples stomatal dynamics to photosynthesis [*Ball et al.*, 1987]:

$$g_s = m\frac{A_n h_s}{C_s} + b_0. \quad (9)$$

The slope (m) and intercept (b_0) are empirically determined parameters. Leaf energy balance is calculated using a linearized form of the leaf energy budget [*Campbell and Norman*, 1998], and the iterative technique of *Tracy et al.* [1984].

[17] Soil respiration flux (f_r) was modeled as an exponential function of soil temperature (T_s),

$$f_r = R_{10} \cdot \exp\left[308.56 \cdot \left(\frac{1}{56.02} - \frac{1}{T_s - 227.13}\right)\right], \quad (10)$$

with R_{10} the respiration rate at 10°C [*Lloyd and Taylor*, 1994]. Energy fluxes at the soil surface were calculated from algorithms presented by *Noilhan and Mahfouf* [1996].

[18] Six model parameters, associated with photosynthetic uptake (V), canopy turbulent dispersion (α and C_d), radiation interception (β), stomatal conductance (m) and soil respiration (R_{10}), were chosen to study the effects of parameter error on model error structures. These six parameters will be referred to as candidate parameters in the following methodological description. The control values used for these parameters were

$$\mathbf{p}^c = \left\{V^c, \alpha^c, C_d^c, \beta^c, m^c, R_{10}^c\right\} = \{59, 0.1, 0.2, 1.0, 5.9, 1.8\}, \quad (11)$$

with units of [μmol CO_2 m^{-2} s^{-1}], dimensionless, dimensionless, dimensionless, dimensionless, and [μmol CO_2 m^{-2} s^{-1}], respectively. As a demonstration of the effect of individual parameter perturbations on model solutions, Figure 4 presents the sensitivities of CO_2 source/sink strength profiles (**s**) and CO_2 concentration profiles (**c**) to ±15% variations of $\mathbf{p}^c$, under typical daytime conditions. The plots also show the effects of varying Q from 600 to 1400 μmol m^{-2} s^{-1}. The patterns produced by each parameter perturbation are examples of the unique error fingerprints placed on model solutions by individual parameter errors. These patterns may change with environmental conditions and the magnitude of the perturbation. Perturbations to α, C_d and R_{10} have a negligible impact on **s** relative to the effect of perturbing V, β or m, which have strong impacts on the vertical **s** distribution and magnitude.

2.2. Determination of Characteristic Error Patterns (CEPs)

2.2.1. General Overview

[19] The approach to error detection presented here centers on the generation of the vertical patterns in CO_2 profile predictions associated with specific parameter errors. Figure 5 provides a schematic diagram of the process by which these error patterns, referred to here as characteristic error patterns (CEPs), are produced. One set of CEPs are produced for each parameter, or parameter combination, suspected as being the primary error source(s) in the model. Two instances of the MLCPM are used in this process. The control model is the MLCPM with default parameter values, assumed to be the true values when generating the CEPs. The perturbed model is identical to the control model, with the exception that one or more parameter values are perturbed from their default values. An ensemble of environmental conditions is used to force both instances of the MLCPM, with the resulting concentration profiles differenced to produce a residual profile set associated with the erroneous parameter value(s) of the perturbed model. The residual profile set is then decomposed using EOF analysis into a set of orthogonal patterns, the CEPs, which optimally characterize the model error structures associated with these parameter(s). The following subsections describe each element in the process of CEP generation, as well as specific aspects associated with the synthetic experiments designed to test the method.

2.2.2. Forcing Ensemble and Environmental Classification

[20] A forcing ensemble, **F**, is defined here as a set of forcing vectors in which the variable values in each vector have been randomly drawn from within realistic ranges to produce forcing conditions under which the broad response of the MLCPM may be tested. The ranges of the environmental variables in **F** may be subdivided into G classes, $\mathbf{F} = \cup_{g=1}^{G}\mathbf{F}^g$, for which system behavior is expected to differ. Error detection may then be performed separately for each environmental class (or simply class in the remainder of the paper), with certain classes potentially advantageous for the isolation of specific error sources.

[21] In the experiments described below, Q, U and air temperature (T_a) values are drawn uniformly from specified ranges to produce forcing ensembles. The ranges of Q and U were determined based on the transitions of ω_1 and ω_2 in the Duke Forest pine application results displayed in Figure 2.

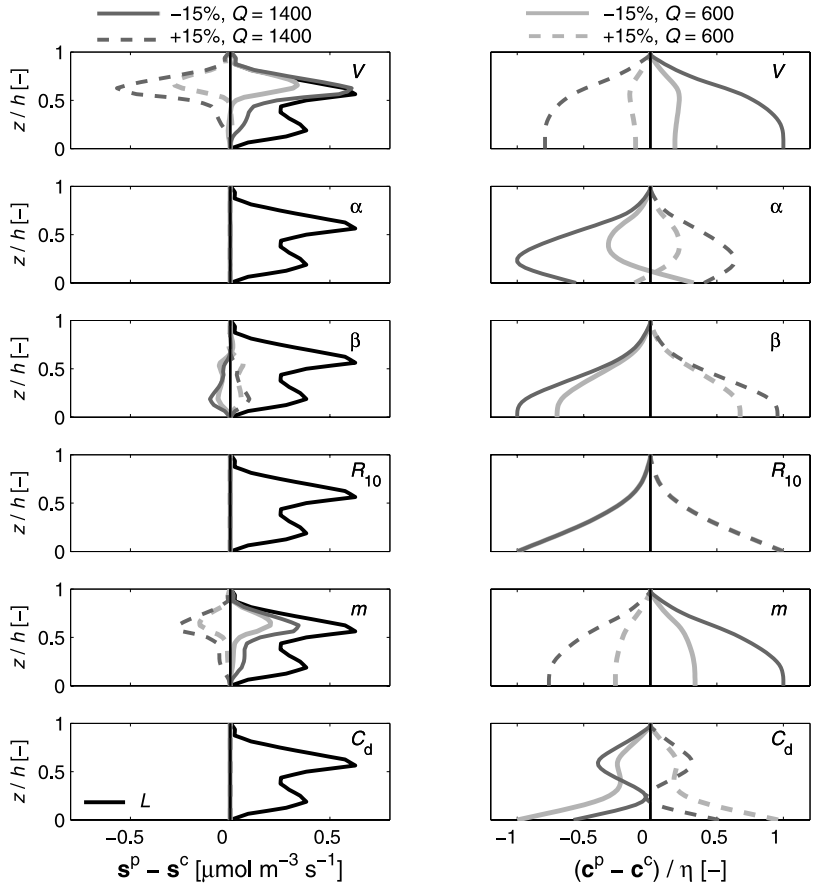

Figure 4. Example perturbation profiles of (left) CO_2 source/sink strength and (right) CO_2 concentration for each of the six CPs. Parameter values were varied by +15% (dashed lines) and −15% (solid lines) of the control values. The concentration perturbation profiles are normalized by η, the absolute maximum value of the perturbation profiles for each CP. For presentation, L is plotted for reference on the source/sink perturbation plots as a black line. Conditions assigned for the simulation runs are as follows: day of year 200, hour 1300, 26% soil moisture, and soil temperature = 18 [°C], with canopy top forcing values of T_a = 22 [°C], vapor pressure = 1.4 [kPa], CO_2 concentration = 360 [ppm], U = 1.2 [m s^{-1}], and Q = 600 (light gray lines) and 1400 (dark gray lines) [μmol m^{-2} s^{-1}].

The values of Q were divided into four ranges ($Q \leq 100$, $100 < Q \leq 500$, $500 < Q \leq 1350$, and $Q > 1350$) [μmol m^{-2} s^{-1}]. Likewise, U values were divided into four ranges ($U \leq 0.4$, $0.4 < U \leq 1.1$, $1.1 < U \leq 2.5$, and $U > 2.5$) [m s^{-1}]. Air temperature values were drawn from the range 18–25 [°C]. Values that remained static in all simulations conducted in this study were: DOY = 200, hour = 13:00, vapor pressure = 1.4 [kPa], soil moisture = 26 [%] and soil temperature = 18 [°C]. Several of these environmental variables could have been varied to further partition environmental classes, as described below. For the purpose of demonstration we chose to vary Q, U and T_a in this study.

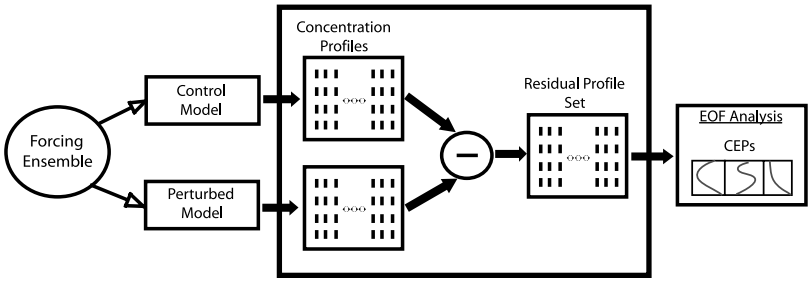

Figure 5. Schematic of the process by which characteristic error patterns (CEPs) are produced. An ensemble of environmental forcing values is used to force both the control and perturbed models. The corresponding concentration profiles produced by each model are differenced to form the residual profile set. The residuals are then EOF analyzed to produce the CEPs.

Table 1. Environmental Classification Based on EOF Analysis of Duke Forest CO_2 Profile Data

	$Q \leq 100$	$100 < Q \leq 500$	$500 < Q \leq 1350$	$Q > 1350$
$U \leq 0.4$	(1,1)	(1,2)[a]	(1,3)[a]	(1,4)
$0.4 < U \leq 1.1$	(2,1)	(2,2)	(2,3)[a]	(2,4)
$1.1 < U \leq 2.5$	(3,1)	(3,2)	(3,3)[a]	(3,4)[a]
$U > 2.5$	(4,1)	(4,2)	(4,3)	(4,4)

[22] Five classes of Q and U were chosen for the experimental tests and are indicated in Table 1. Of the 16 Q/U classes, we limit our discussion here to daytime values in which the canopy is not well mixed, eliminating the regions in which $Q \leq 100$ and $U > 2.5$. Of the remaining classes, we focus on the five in which most data fall, as wind speeds typically increase during the day with radiation. These five classes are indicated in Table 1.

2.2.3. Forward Model

[23] The MLCPM, or simply the forward model (f), accepts as input an ensemble of environmental forcing conditions, $\mathbf{F} = \{\mathbf{f}_i | i = 1,\ldots,n_f\}$, and a vector of component submodel parameter values, $\mathbf{p} = \{p_i | i = 1,\ldots,n_p\}$. Each vector $\mathbf{f}$ in the forcing ensemble contains the values of the meteorological variables and other environmental inputs necessary to run the MLCPM. The forward model produces as output a set of CO_2 concentration profiles, $\mathbf{D} = \{\mathbf{d}_i | i = 1,\ldots, n_f\}$, one for each forcing vector:

$$\mathbf{D} = \mathrm{f}(\mathbf{F}, \mathbf{p}). \tag{12}$$

2.2.4. Control Profile Set

[24] MLCPM formulations require a large number of component submodel parameters, each with some level of uncertainty and temporal variability. A subset of these are chosen to be the candidate parameters (CPs), those parameters whose values have a large degree of uncertainty, are known to vary considerably, or for which the sensitivity of model outputs is high. The CPs have control values, $\mathbf{p}^c = \{p_i^c | i = 1,\ldots,n_c\}$ (see equation (11)), where n_c is the number of CPs. The set of control profiles produced by running the forward model with $\mathbf{F}$ and $\mathbf{p}^c$, i.e., $\mathbf{D}^c = \mathrm{f}(\mathbf{F},\mathbf{p}^c)$, is

$$\mathbf{D}^c = \begin{bmatrix} d^c(1,1) & \cdots & d^c(1,n_f) \\ \vdots & & \vdots \\ d^c(r,1) & \cdots & d^c(r,n_f) \end{bmatrix} = \left[\mathbf{d}_1^c, \ldots, \mathbf{d}_{n_f}^c\right]. \tag{13}$$

2.2.5. Perturbed Parameter Sets

[25] An input parameter vector for the perturbed model, $\mathbf{p}^p$, is identical to $\mathbf{p}^c$ with a subset of the CPs, $\mathbf{n} \subset \mathbf{p}^c$, perturbed a fractional amount δ. Each CP has a range of allowable perturbations from which δ is drawn uniformly. A unique value of δ is drawn for each member of $\mathbf{f}$ and each perturbed parameter. Maximum perturbation magnitudes for each CP are based on knowledge of reasonable ranges of the CPs, or the degree to which model outputs are sensitive to perturbations. An example of a perturbation vector with $\mathbf{n} = \{\mathbf{p}_i^c\}$ is given in equation (14), and the entire set of perturbation vectors necessary to produce the perturbed profile set, $\mathbf{D}_\mathbf{n}^p = \mathrm{f}(\mathbf{F},\mathbf{P}_\mathbf{n}^p)$, is given in equation (15).

$$\mathbf{p}_{\mathbf{n},j}^p = \left\{p_1^c, \ldots, p_i^c + \delta_{i,j} p_i^c, \ldots, p_{n_c}^c | i \in 1,\ldots,n_c; j \in 1,\ldots,n_f\right\} \tag{14}$$

$$\mathbf{P}_\mathbf{n}^p = \left[\mathbf{p}_{\mathbf{n},1}^p, \ldots, \mathbf{p}_{\mathbf{n},n_f}^p\right] \tag{15}$$

[26] In the synthetic experiments performed in this paper, the maximum perturbation magnitude assigned to V was 30% [*Ellsworth*, 2000]. The maximum perturbation magnitudes of the remaining CPs were found by varying the perturbation magnitude until the mean vertically summed absolute difference (perturbed – control profiles), for an ensemble of 1000 random forcing sets, across the entire range of forcing data used in this study, was found to be nearly identical to that produced by a 30% perturbation in V. The set of maximum perturbation magnitudes for the CP set, $\{V^c, \alpha^c, \beta^c, R_{10}^c, m^c, C_d^c\}$, was found to be {30, 8, 33, 25, 21, 75} [%]. The magnitudes were chosen in this way to produce comparable profile perturbations for testing with multiple CP basis sets for cases of interacting parameters. When parameter perturbations are applied, positive and negative perturbations are equally likely.

2.2.6. Residual Profile Sets and Characteristic Error Patterns

[27] The residual profile set is the difference $\mathbf{R}_\mathbf{n} = \mathbf{D}_\mathbf{n}^p - \mathbf{D}^c$. The CEPs of the CP subset $\mathbf{n}$ are produced by an EOF analysis of $\mathbf{R}_\mathbf{n}$. The mutually orthogonal CEPs can be used to fully reconstruct the qth residual profile, $\mathbf{r}_q$, in $\mathbf{R}_\mathbf{n}$ as in equation (16).

$$\mathbf{r}_q = \sum_{k=1}^{r} \omega_k(q)\phi_{\mathbf{n},k} \tag{16}$$

The full set of CEPs of $\mathbf{n}$, $\mathbf{\Phi}_\mathbf{n} = [\phi_{\mathbf{n},1},\ldots,\phi_{\mathbf{n},r}]$, form a complete basis for all vectors in $\mathbf{R}_\mathbf{n}$. The optimality of EOF analysis retains the bulk of the information about the error structures in the first few CEPs, allowing the remaining patterns to be truncated:

$$\mathbf{r}_q \approx \sum_{k=1}^{s} \omega_k(q)\phi_{\mathbf{n},k} \quad (s < r). \tag{17}$$

The construction of the CEPs described above is performed for each environmental class separately, forming class-specific CEP sets, $\mathbf{\Phi}_\mathbf{n}^g$.

2.3. Primary Error Determination

[28] The CEP sets described above are the unique error structures associated with each CP or CP combination. Each CEP set has the property of being a set of mutually orthogonal vectors, providing a convenient basis onto which other vectors of the same length may be projected. Difference concentration profiles are calculated as $\mathbf{D}^d = \mathbf{D}^c - \mathbf{D}^m$, where $\mathbf{D}^m$ is a set of measured profiles, and $\mathbf{D}^c$ is a set of modeled profiles using the default parameter set, $\mathbf{p}^c$, and the measured environmental forcing. The difference profiles provide a source of information on the vertical structure of MLCPM error. The CEP sets condense this information

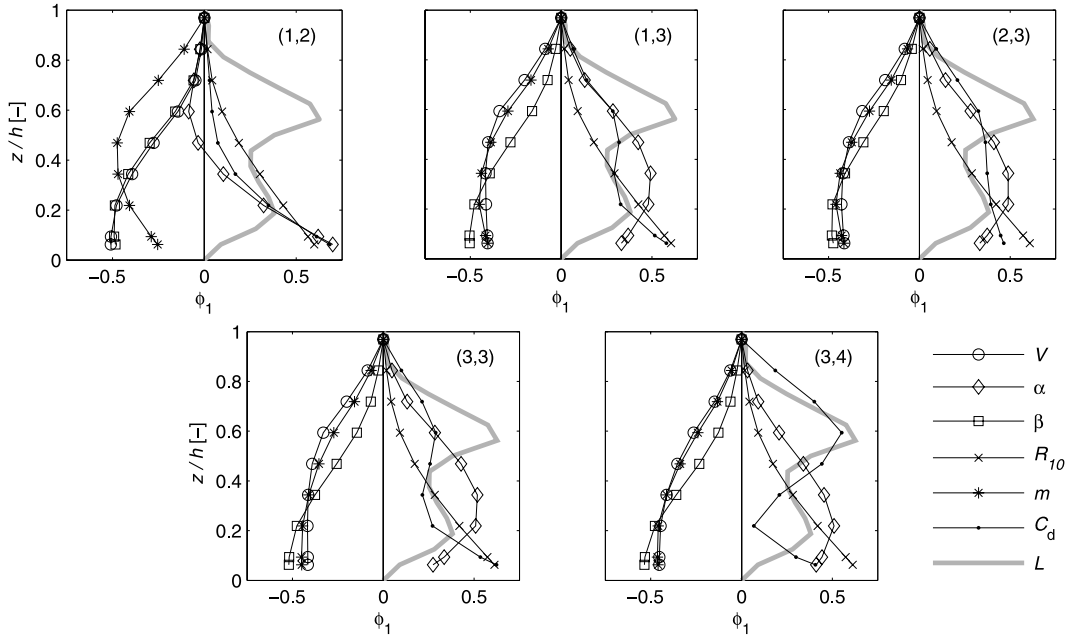

Figure 6. First EOF for the single-CP cases. Environmental class labels (top right corners) correspond to the labels in Table 1.

into a few vertical patterns associated with a CP or CP combination.

[29] Primary error sources are determined by projecting each difference profile, **d**, in $\mathbf{D}^d$ separately onto each CEP set. The approximation of **d** by projection onto the basis specified by the parameter subset **n**, composed of *j* basis vectors, for the *g*th environmental class, is given by

$$\tilde{\mathbf{d}}^{\mathbf{n}} = \sum_{j} \left\langle \mathbf{d}, \phi^{g}_{\mathbf{n},j} \right\rangle \phi^{g}_{\mathbf{n},j}, \tag{18}$$

where the brackets represent a vector dot product.

[30] The basis set which best reconstructs the vectors in $\mathbf{D}^d$ is determined to be the primary error source. Accuracy of the reconstruction of a profile in this paper is quantified using the L-2 norm:

$$\varepsilon_i = \| \mathbf{d} - \tilde{\mathbf{d}}^i \|_2 . \tag{19}$$

The primary error source contributing to the error residual is determined to be the CP set having the minimum ε value. We note that several other valid choices for the criterion describing the accuracy of the reconstruction exist [*Janssen and Heuberger*, 1995].

3. Results

[31] We examine the ability of the error patterns associated with each CP, and CP pairs, to identify sources of parameter error due to single and paired parameter perturbations. Three synthetic tests of the method were performed. The advantage of synthetic tests is that the true source of model error is known, allowing conclusions to be drawn about the effectiveness of the method. Synthetic testing also allows focus to be placed on the specific aspect of the error detection problem addressed here, the identification of model bias caused by errors in parameter values, excluding the complicating factors of measurement and model structural errors. Each test required a forcing ensemble, which was used to create a synthetic truth (referred to hereafter as measured) and a perturbed (referred to hereafter as modeled) profile ensemble.

[32] Two synthetic tests were performed using the six single-CP basis sets. The CEPs were generated using forcing ensembles of 1000 members for each environmental class studied here (see Table 1). The first EOFs of each CP, in each of the environmental classes, are displayed in Figure 6. The patterns associated with certain parameters distinguish themselves under specific environmental conditions. For example, the patterns associated with *V* and *m* are best distinguished in class (1,2), while those of *V* and β are better distinguished under higher radiation conditions. The importance of determining the classes for which parameter errors are best distinguished will be demonstrated below.

[33] The percentage of variability accounted for by the first 3 EOFs for each class is presented in Table 2. The first two EOFs account for >94% of the data set variability in all cases, with >98% accounted for by ϕ_1 and ϕ_2 in all but two cases. The addition of ϕ_3 added a negligible amount of data set variability. We therefore limit the error projection basis sets (CEPs) to the first two EOFs.

[34] The initial set of synthetic test profiles was produced by inducing error in a single model parameter. A new 1000-member forcing ensemble for each environmental class was used to create the measured and modeled profile sets. The percentage of identifications (IDs) made for each basis set is presented in Table 3, organized by error source (ES) and environmental class. Correct identification percentages are indicated in bold. Italic percentages denote the cases in which one or more basis sets other than that of the actual ES had the highest score. This occurred in only two instances: β as the ES in class (1,2) and *m* as the ES in class (3,4). In both cases the method identified *V* as the most likely source

Table 2. Percentage of Variability Described by the First Three CEPs of the Six CPs Used in This Study for Each Environmental Class[a]

Parameter	EOF 1	EOF 2	EOF 3	EOF 1+2
		Class (1,2)		
V	86.83	11.91	1.26	98.74
α	90.02	9.78	0.17	99.8
β	97.55	2.35	0.09	99.9
R_{10}	99.93	0.07	0	100
m	75.97	23.96	0.07	99.92
C_d	98.24	1.37	0.31	99.61
		Class (1,3)		
V	99.47	0.49	0.03	99.96
α	96.64	3.06	0.19	99.7
β	99.47	0.52	0	99.99
R_{10}	99.82	0.17	0	100
m	99.35	0.61	0.04	99.96
C_d	86.89	7.81	4.7	94.7
		Class (2,3)		
V	99.45	0.45	0.09	99.91
α	96.91	2.97	0.11	99.89
β	96.32	3.68	0	100
R_{10}	99.19	0.81	0	100
m	99.49	0.47	0.04	99.96
C_d	83.44	12.98	3.57	96.42
		Class (3,3)		
V	99.53	0.47	0	100
α	94.9	5.08	0.02	99.98
β	99.98	0.02	0	100
R_{10}	100	0	0	100
m	99.72	0.25	0.04	99.96
C_d	91.32	7.22	1.44	98.54
		Class (3,4)		
V	99.89	0.08	0.02	99.98
α	99.88	0.12	0	100
β	99.99	0.01	0	100
R_{10}	100	0	0	100
m	99.63	0.36	0.01	99.99
C_d	91.28	7.45	1.24	98.73

[a]See Table 1.

of model bias. This agrees with the observation made above, that the first CEP of V is not uniquely distinguished from these two parameters in these environmental classes. This may be explained by the tight coupling between the Ball-Berry stomatal conductance model and Farquhar-based photosynthesis model in the MLCPM, with $g_s = f(A_n)$, $A_n = f(c_i)$, and $c_i = f(g_s)$. The functional interdependencies of these two submodels, and the fact that radiation drives both, may produce similar error profiles under specific conditions. It is important to note, however, that the patterns become well distinguished as radiation increases (for V and β) or decreases (for V and m). For all other ESs, and classes, the error source was unambiguously identified correctly.

[35] The second test used the same set of single-CP basis sets for the projection of error vectors that were produced with two embedded error sources. Again, a new forcing ensemble was used to produce 1000 error profiles (modeled minus measured) for each environmental class and each two-parameter combination. The primary error source (PES) for each profile was determined to be the ES whose error profile, using only the ES as a single error source under identical environmental conditions, had the greatest absolute sum. The other ES will be referred to as the secondary error source (SES). For this test the data were filtered so that the absolute difference in the error produced by the PES and the SES was at least 50% that of the PES, representing cases in which the PES was dominant. Table 4 presents the percentage of IDs made for each PES/class combination. The results are similar to the single-ES case, as the only two cases for which the PES was not unambiguously identified were β in class (1,2) and m in class (3,4). Generally, the percentage of correct IDs decreased when a second error source was included. This is expected, as the second error source acts, through the action of the MLCPM, to nonlinearly adjust the residual profiles, potentially to an extent that error profiles do not resemble the single CP basis sets. EOF analysis is a linear transformation, ideal for the separation of modes that are linearly independent of each other. Multiple error sources in an MLCPM will likely produce a nonlinear combination of the two individual error sources, due to the nonlinear relationships inherent in MLCPM formulations.

[36] The same results, organized in terms of PES and SES pairs, are presented in Table 5, where correct IDs were made for all but the following PES/SES pairs: (V/C_d), (β/α), (β/C_d), (R_{10}/C_d), (m/β) and (m/C_d). The last two columns of Table 5 present the maximum correct ID percentage and the class in

Table 3. Percent IDs for a Single Error Source and Single-CP Basis Sets[a]

		Basis Sets					
ES	Class	V	α	β	R_{10}	m	C_d
V	(1,2)	**47.84**	8.78	6.23	30.53	6.62	0
V	(1,3)	**94.5**	0	1.53	0.31	3.56	0.1
V	(2,3)	**89.25**	0	0.52	0	0.72	9.51
V	(3,3)	**99.09**	0	0	0.1	0.81	0
V	(3,4)	**99.7**	0	0	0.2	0.1	0
α	(1,2)	0	**55.46**	9.35	16.59	14.14	4.45
α	(1,3)	0.85	**62.79**	3.52	22.6	8.64	1.6
α	(2,3)	0	**66.81**	1.6	3.3	17.55	10.74
α	(3,3)	0	**96.88**	0	2.41	0.4	0.3
α	(3,4)	0	**99.4**	0	0.4	0.2	0
β	(1,2)	51.56	6.72	*33.5*	6.1	0.62	1.49
β	(1,3)	0	0	**99**	0.4	0.6	0
β	(2,3)	0	0.72	**99.28**	0	0	0
β	(3,3)	0	3.02	**94.67**	1.01	1.31	0
β	(3,4)	0	0	**99.09**	0.2	0.71	0
R_{10}	(1,2)	0	1.81	0	**85.8**	12.39	0
R_{10}	(1,3)	0	0	0	**99.1**	0.9	0
R_{10}	(2,3)	0	0	0	**100**	0	0
R_{10}	(3,3)	0	0	0	**99.9**	0	0.1
R_{10}	(3,4)	0	0	0	**99.9**	0.1	0
m	(1,2)	8.66	0.21	2.68	0.1	**88.25**	0.1
m	(1,3)	15.09	0.11	22.48	0.43	**61.89**	0
m	(2,3)	32.63	0	2.34	1	**62.36**	1.67
m	(3,3)	34.61	0	0	4.86	**60.42**	0.12
m	(3,4)	54.45	0	0	1.3	*44.25*	0
C_d	(1,2)	0	7.75	0.44	23.69	0.33	**67.79**
C_d	(1,3)	8.23	11.05	0.23	4.74	9.02	**66.74**
C_d	(2,3)	7.68	5.67	0	0.22	14.91	**71.52**
C_d	(3,3)	0.1	5.82	0	0.42	2.39	**91.28**
C_d	(3,4)	0	1.6	0	0.2	0	**98.2**

[a]Data are organized according to error source (ES) and the environmental classes (Class) in Table 1. Italic and bold percentages correspond to correct projections, those for which the correct error source (ES) was identified. Bold represents those cases in which the correct identification was made more than any other CP identification. Italic percentages are those cases for which at least one CP other than the ES was identified more frequently than the ES.

Table 4. Same as Table 3 for the Case of Two Embedded Error Sources and Single-CP Basis Sets

		Basis Sets					
PES	Class	V	α	β	R_{10}	m	C_d
V	(1,2)	**30.71**	20.35	12.57	25.45	8.09	2.83
V	(1,3)	**63.08**	4.15	9.24	1.99	14.75	6.78
V	(2,3)	**53.08**	4.17	5.44	1.66	9.36	26.29
V	(3,3)	**59.31**	4.49	0.41	2.94	16.61	16.24
V	(3,4)	**59.56**	4.77	0.34	3.72	15.63	15.99
α	(1,2)	0.27	**52.05**	10.14	14.08	19.01	4.44
α	(1,3)	4.51	**41.66**	12.39	20.36	13.47	7.61
α	(2,3)	2	**51.74**	5.24	7.09	17.75	16.19
α	(3,3)	2.18	**79.88**	0.1	10.03	4.84	2.98
α	(3,4)	6.32	**66.64**	5.48	5.39	4.05	12.13
β	(1,2)	39.23	8.2	*32.61*	13.1	3.91	2.96
β	(1,3)	12.15	5.98	**47.63**	18.67	11.51	4.06
β	(2,3)	12.94	30.01	**38.65**	11.18	5.95	1.27
β	(3,3)	8.38	29	**42.23**	13.39	6.58	0.41
β	(3,4)	12.5	18.53	**37.1**	8.6	15.37	7.91
R_{10}	(1,2)	1.03	21.02	2.51	**40.87**	29.63	4.95
R_{10}	(1,3)	3.59	0.69	9.82	**62.95**	21.47	1.47
R_{10}	(2,3)	2.5	23.91	6.89	**58.15**	8.21	0.35
R_{10}	(3,3)	1.52	13.35	6.57	**62.46**	15.94	0.15
R_{10}	(3,4)	10.72	5.62	0	**66.68**	16.75	0.23
m	(1,2)	18.63	4.96	13.59	2.85	**55.74**	4.23
m	(1,3)	15.64	6.52	29.68	6.22	**33.09**	8.86
m	(2,3)	21.66	8.86	11.31	13.61	**30.52**	14.03
m	(3,3)	20.07	8.08	2.17	24.11	**42.19**	3.38
m	(3,4)	34.09	5.79	0.74	13.53	*23.85*	22.01
C_d	(1,2)	0.09	9.24	0.81	27.51	2.54	**59.82**
C_d	(1,3)	7.1	15.22	1.23	11	17.64	**47.8**
C_d	(2,3)	6.15	9.05	0.17	0.53	23.75	**60.35**
C_d	(3,3)	2.33	9.4	0.03	1.18	9.37	**77.68**
C_d	(3,4)	0.96	6.57	0.07	0.66	0.66	**91.06**

which it was made for each PES/SES pair. In each case the maximum was a correct ID of the PES for that class, demonstrating the effectiveness of environmental classification in separating tangled error influences. Figure 7 displays the fraction of correct IDs (f_{cid}) versus Q (Figure 7, left) and U (Figure 7, right). The fraction of correct IDs were binned in 50 [μmol m^{-2} s^{-1}] and 0.1 [m s^{-1}] bins for Q and U, respectively. Viewing the projection results in this manner can help better specify environmental classes. For example, m is best identified in the center of each Q range, and the performance of V decreases with decreasing Q in the first Q range, pointing to potentially improved class demarcations where CEP sets focused on a smaller range of environmental conditions could improve performance.

[37] The final tests utilized the single-CP basis sets from the previous two tests, as well as CEP sets derived from pairs of CPs. The two-CP basis sets were produced in an identical manner as that of the single-CP CEPs, with simultaneous perturbations applied to each CP. Error magnitudes were drawn uniformly from the error ranges for each parameter independently, with both positive and negative perturbations equally likely.

[38] We examine the performance of two-CP basis sets for three of the interacting ES cases for which correct IDs were not made in the single-CP experiments (see Table 5): (β/α), (m/β) and (m/C_d). All six single-CP basis sets were used, as well as six two-CP basis sets composed of pairs of the four CPs most identified for each of these cases in Table 5. The data from the previous two-error-source tests were used. The results are organized by environmental class in Table 6. The β/α and m/C_d CEPs performed well, with three environmental classes providing correct IDs. The m/β CEPs, however, only produced a correct ID in one environmental class. This is likely due to the tight coupling of m, β and V, as discussed previously. These results suggest this combined error source might best be identified under low-wind/intermediate-radiation conditions, where m and β individually distinguished themselves from V.

4. Conclusions

[39] This paper presents a method by which structural (spatial) patterns in model outputs can be identified and associated with errors in one or more parameter values. The method centers on the use of EOF analysis to produce sets of orthogonal patterns that capture the majority of the variability associated with specific parameter biases. The orthogonal nature of the EOFs allows them to naturally form basis sets onto which model/data residuals may be projected and reconstructed. The method is applied to the identification of the primary source(s) of parameter error in modeled canopy sublayer CO_2 concentration profiles through a set of single and multiple error source synthetic cases. The demonstration focuses on CO_2 profiles, but the approach is readily applied to humidity and temperature profiles as well.

Table 5. Percent IDs for the Case of Two Embedded Error Sources and Single-CP Basis Sets, Organized According to Primary Error Source and Secondary Error Source[a]

		Basis Sets							
PES	SES	V	α	β	R_{10}	m	C_d	Max	Class
V	α	**40.6**	1.59	3.86	3.98	23.58	26.39	61.68	(1,3)
V	β	**74.66**	2.09	1.72	3.89	14.57	3.06	86.77	(3,4)
V	R_{10}	**45.14**	0.68	9.28	4.06	34.22	6.62	53.1	(3,4)
V	m	**81.26**	4.96	2.91	5.51	2.71	2.65	99.24	(3,4)
V	C_d	*28.59*	16.05	4	6.51	7.16	37.7	47.47	(1,3)
α	V	0.21	**53.89**	7.99	16.7	14.9	6.32	72.71	(3,4)
α	β	0.07	**69.98**	5.18	10.23	11.62	2.92	99.05	(3,4)
α	R_{10}	0.7	**61.99**	15.45	8.88	9.83	3.15	87.07	(3,3)
α	m	0.04	**68.81**	4.72	11.25	10.14	5.05	91.88	(3,3)
α	C_d	14.14	**32.92**	5.36	9.78	13.61	24.19	59.2	(3,3)
β	V	20.19	10.18	**42.47**	17.7	7.75	1.71	50.31	(1,3)
β	α	3.56	45.4	*31.61*	17.47	1.78	0.17	86.13	(3,4)
β	R_{10}	4.14	29.19	**52.85**	9.73	3.69	0.39	66.67	(3,4)
β	m	18.35	15.22	**57.21**	8.42	0.44	0.36	84	(1,3)
β	C_d	26.85	10.07	*13.54*	14.33	24.52	10.7	47.89	(1,2)
R_{10}	V	0.24	19.11	6.44	**49.26**	22.03	2.91	92.57	(3,4)
R_{10}	α	1.08	26.47	5.73	**57.08**	8.97	0.68	100	(3,4)
R_{10}	β	0.05	4.29	0.11	**80.65**	12.4	2.5	99.69	(3,4)
R_{10}	m	0.06	16.08	0.6	**67.32**	15.91	0.02	99.81	(3,4)
R_{10}	C_d	14.5	9.61	13.27	*23.65*	35.68	3.29	46.18	(1,2)
m	V	29.81	4.07	16.77	11.17	**35.82**	2.35	54.95	(1,2)
m	α	5.99	3.24	12.38	16.99	**54.21**	7.2	73.93	(3,4)
m	β	41.77	1.03	15.68	12.33	*28.21*	0.98	55.64	(1,2)
m	R_{10}	8.44	0.19	15.81	18.48	**54.54**	2.54	80	(1,2)
m	C_d	16.24	19.04	5.45	6.13	*17.75*	35.39	60.47	(1,2)
C_d	V	1.18	11.4	0.6	12.76	11.93	**62.13**	83.98	(3,4)
C_d	α	4.03	8.15	0.36	7.07	13.25	**67.14**	81.89	(3,4)
C_d	β	3.68	9.21	0.5	14.83	8.67	**63.1**	96.3	(3,4)
C_d	R_{10}	4.69	12.66	1.15	12.26	8.97	**60.27**	86.79	(3,4)
C_d	m	2.49	8.73	0.27	11.54	8.83	**68.15**	96.28	(3,4)

[a]The last two columns display the maximum fraction of correct IDs, and the environmental class for which the maximum occurred. Bold and italics have the same meaning as in Table 3.

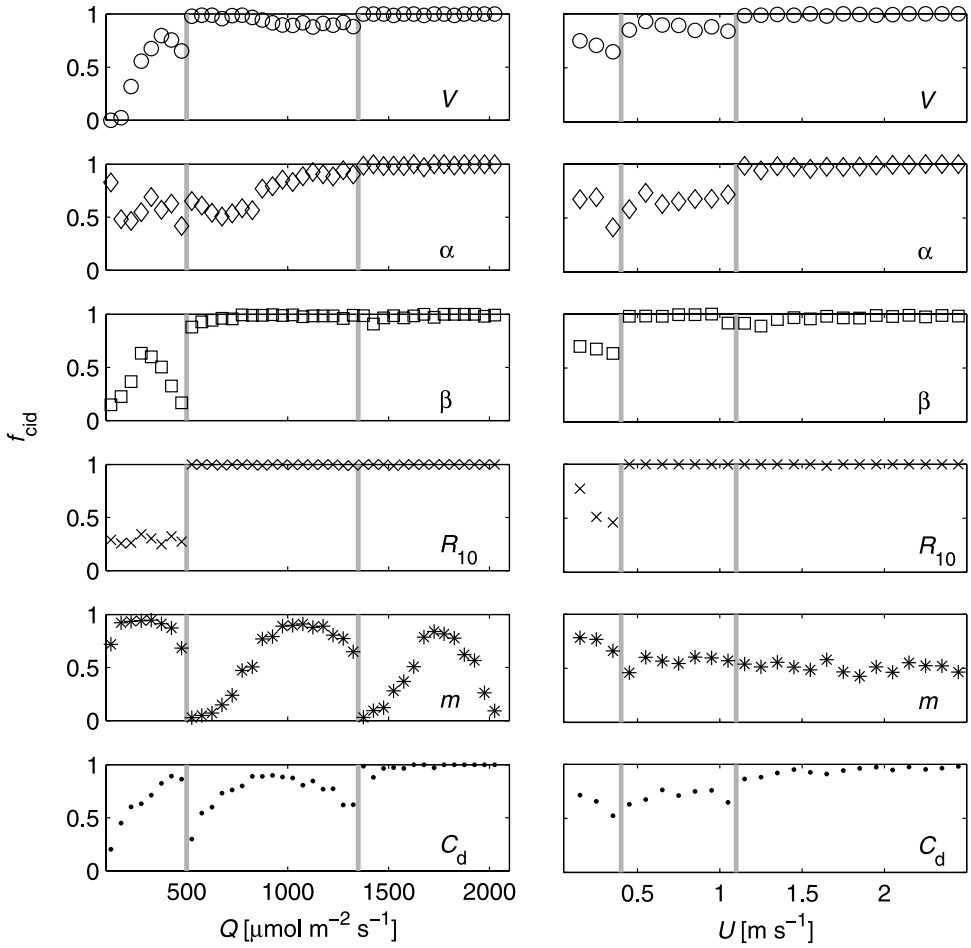

Figure 7. Fraction of correct IDs (f_{cid}) for the two-error-source case projected onto single-CP basis sets. Q and U are binned into 50 [μmol m^{-2} s^{-1}] and 0.1 [m s^{-1}] bins, respectively.

Table 6. Results From the Case of Two Embedded Error Sources and Single- and Double-CP Basis Sets, Organized According to Primary Error Source Pairs and Environmental Class

		Basis Sets											
PES Pair	Class	V	α	β	R_{10}	m	C_d	V/α	V/β	V/R_{10}	β/α	α/R_{10}	β/R_{10}
β/α	(1,2)	0	4.65	12.5	11.06	8.81	1.92	9.13	0.48	9.62	**24.2**	5.61	12.02
β/α	(1,3)	1.32	8.88	2.74	22.59	4.5	0.11	5.15	0.11	1.97	*17.43*	17.54	17.65
β/α	(2,3)	3.77	40.9	0.54	2.15	1.08	2.91	11.73	0.32	0.11	*1.4*	33.8	1.29
β/α	(3,3)	0	20.22	0	1.63	0.1	0	3.35	0.1	0	**44**	30.39	0.2
β/α	(3,4)	0.39	2.2	0	1.03	1.16	0	0.13	0.13	0	**77.52**	17.44	0
		Basis Sets											
PES Pair	Class	V	α	β	R_{10}	m	C_d	V/β	V/R_{10}	V/m	β/R_{10}	m/β	R_{10}/m
m/β	(1,2)	12.54	7.86	8.86	1.34	0.5	0.67	28.6	5.85	13.04	0.5	*14.55*	5.69
m/β	(1,3)	0.82	0	14.55	8.69	2.58	0.12	25.59	3.05	6.1	0.47	**33.69**	4.34
m/β	(2,3)	3.71	0	0.72	9.21	1.2	0	39.23	0.24	32.18	0.6	*0.36*	12.56
m/β	(3,3)	3.4	0	0.12	4.46	0.23	1.53	88.5	0.12	0	0.12	*0*	1.53
m/β	(3,4)	5.16	0	0	9.18	0	0	57.59	0	0.62	0	*24.87*	2.58
		Basis Sets											
PES Pair	Class	V	α	β	R_{10}	m	C_d	V/α	V/m	V/C_d	α/m	α/C_d	m/C_d
m/C_d	(1,2)	0.57	2.87	2.87	6.88	6.88	14.04	2.58	1.43	8.02	5.44	4.58	**43.84**
m/C_d	(1,3)	10.1	3.71	1.93	3.27	2.53	30.16	11.29	0.3	18.13	3.71	4.9	*9.96*
m/C_d	(2,3)	5.07	1.55	0	0.14	0.99	15.63	1.83	0	16.62	0.42	19.58	**38.17**
m/C_d	(3,3)	5.56	5.16	0	0	0.27	18.32	6.38	0	12.75	0.41	35.69	*15.47*
m/C_d	(3,4)	0	0.42	0	0.42	0	8.06	16.39	0	12.92	1.39	25.69	**34.72**

[40] The results demonstrated significant skill in identifying the primary source of model error when one source of bias was present. Single candidate parameter (CP) basis sets showed strong performance with two embedded error sources, when one source was dominant. As well, basis sets formed with pairs of interacting parameters were used with success to identify combined error sources of comparable magnitude, nonlinearly mixed by the MLCPM.

[41] The ability of the method to resolve model error will likely be dependent on the selection of the CP set and the environmental classification used, as coupling between submodels may cause parameter errors to form similar error patterns. The classification of environmental conditions was demonstrated to be effective at separating errors in coupled model parameters (i.e., V, β and m). The classification scheme used in this paper was based on a principal components analysis of measured concentration profiles. In practice, data analysis provides a method for obtaining general classification boundaries. This can be used in conjunction with a detailed sensitivity analysis of the model, such as that performed in the synthetic experiments in this paper, to further specify class boundaries useful for resolving the effects of strongly coupled parameters. While, for demonstration purposes, the classification scheme in this paper was focused solely on Q and U, other controlling environmental variables such as time of day, season, air temperature, soil moisture status, and vapor pressure deficit may be used to more precisely classify environmental regimes.

[42] The focus of this study was the presentation of the method and initial synthetic testing using CO_2 profiles as an example. The confounding effects of measurement and model structural error provide challenges for future studies. Simultaneous use of multiple scalar profiles (CO_2, T_a, H_2O) is likely to further constrain model error source identifications. Application of techniques such as the one described in this paper could prove useful for higher-dimensional models, such as distributed hydrological models, in which parameter optimization is a critical issue.

[43] **Acknowledgment.** This research was funded by the Office of Science (BER), U.S. Department of Energy, under cooperative agreement DE-FCO3-90ER61010, and the NASA Earth System Science Fellowship program.

References

Baldocchi, D. (1997), Measuring and modelling carbon dioxide and water vapour exchange over a temperate broad-leaved forest during the 1995 summer drought, *Plant Cell Environ.*, *20*(9), 1108–1122.

Baldocchi, D. D., and P. C. Harley (1995), Scaling carbon-dioxide and water-vapor exchange from leaf to canopy in a deciduous forest: 2. Model testing and application, *Plant Cell. Environ.*, *18*(10), 1157–1173.

Baldocchi, D. D., and K. B. Wilson (2001), Modeling CO_2 and water vapor exchange of a temperate broadleaved forest across hourly to decadal time scales, *Ecol Modell.*, *142*(1–2), 155–184.

Baldocchi, D., R. Valentini, S. Running, W. Oechel, and R. Dahlman (1996), Strategies for measuring and modelling carbon dioxide and water vapour fluxes over terrestrial ecosystems, *Global Change Biol.*, *2*(3), 159–168.

Baldocchi, D. D., C. A. Vogel, and B. Hall (1997), Seasonal variation of carbon dioxide exchange rates above and below a boreal jack pine forest, *Agric. For. Meteorol.*, *83*(1–2), 147–170.

Baldocchi, D., K. Wilson, and G. Lianhong (2002), How the environment, canopy structure and canopy physiological functioning influence carbon, water and energy fluxes of a temperate broad-leaved deciduous forest: An assessment with the biophysical model CANOAK, *Tree Physiol.*, *22*, 1065–1077.

Ball, J. T., I. E. Woodrow, and J. A. Berry (1987), A model predicting stomatal conductance and its contribution to the control of photosynthesis under different environmental conditions, in *Progress in Photosynthesis Research*, vol. IV, *Proceedings of the International Congress on Photosynthesis*, edited by J. Biggens, pp. 221–224, Martinus Nihjoff, Zoetermeer, Netherlands.

Beven, K., and J. Freer (2001), Equifinality, data assimilation, and uncertainty estimation in mechanistic modelling of complex environmental systems using the GLUE methodology, *J. Hydrol.*, *249*(1–4), 11–29.

Cai, T., and Q.-L. Dang (2002), Effects of soil temperature on parameters of a coupled photosynthesis-stomatal conductance model, *Tree Physiol.*, *22*, 819–827.

Campbell, G. S., and J. M. Norman (1998), *An Introduction to Environmental Biophysics*, Springer, New York.

Chen, W. J., et al. (1999), Effects of climatic variability on the annual carbon sequestration by a boreal aspen forest, *Global Change Biol.*, *5*(1), 41–53.

Collatz, G. J., J. T. Ball, C. Grivet, and J. A. Berry (1991), Physiological and environmental-regulation of stomatal conductance, photosynthesis and transpiration: A model that includes a laminar boundary-layer, *Agric. For. Meteorol.*, *54*(2–4), 107–136.

Ellsworth, D. S. (1999), CO_2 enrichment in a maturing pine forest: Are CO_2 exchange and water status in the canopy affected?, *Plant Cell Environ.*, *22*(5), 461–472.

Ellsworth, D. S. (2000), Seasonal CO_2 assimilation and stomatal limitations in a *Pinus taeda* canopy, *Tree Physiol.*, *20*(7), 435–445.

Farquhar, G. D., S. V. Caemmerer, and J. A. Berry (1980), A biochemical-model of photosynthetic CO_2 assimilation in leaves of C-3 species, *Planta*, *149*(1), 78–90.

Franks, S. W., K. J. Beven, P. F. Quinn, and I. R. Wright (1997), On the sensitivity of soil-vegetation-atmosphere transfer (SVAT) schemes: Equifinality and the problem of robust calibration, *Agric. For. Meteorol.*, *86*(1–2), 63–75.

Greco, S., and D. D. Baldocchi (1996), Seasonal variations of CO_2 and water vapour exchange rates over a temperate deciduous forest, *Global Change Biol.*, *2*(3), 183–197.

Gu, L. H., H. H. Shugart, J. D. Fuentes, T. A. Black, and S. R. Shewchuk (1999), Micrometeorology, biophysical exchanges and NEE decomposition in a two-story boreal forest: Development and test of an integrated model, *Agric. For. Meteorol.*, *94*(2), 123–148.

Gupta, H. V., L. A. Bastidas, S. Sorooshian, W. J. Shuttleworth, and Z. L. Yang (1999), Parameter estimation of a land surface scheme using multicriteria methods, *J. Geophys. Res.*, *104*, 19,491–19,503.

Hollinger, D. Y., F. M. Kelliher, J. N. Byers, J. E. Hunt, T. M. McSeveny, and P. L. Weir (1994), Carbon-dioxide exchange between an undisturbed old-growth temperate forest and the atmosphere, *Ecology*, *75*(1), 134–150.

Hollinger, D. Y., et al. (2004), Spatial and temporal variability in forest-atmosphere CO_2 exchange, *Global Change Biol.*, *10*(10), 1689–1706.

Hotelling, M. (1933), Analysis of a complex of statistical variables into principal components, *J. Educ. Psychol.*, *24*, 498–520.

Janssen, P. H. M., and P. S. C. Heuberger (1995), Calibration of process-oriented models, *Ecol. Modell.*, *83*(1–2), 55–66.

Katul, G., C. T. Lai, K. Schafer, B. Vidakovic, J. Albertson, D. Ellsworth, and R. Oren (2001), Multiscale analysis of vegetation surface fluxes: From seconds to years, *Adv. Water Resour.*, *24*(9–10), 1119–1132.

Katul, G. G., L. Mahrt, D. Poggi, and C. Sanz (2004), One- and two-equation models for canopy turbulence, *Boundary Layer Meteorol.*, *113*(1), 81–109.

Kuczera, G., and E. Parent (1998), Monte Carlo assessment of parameter uncertainty in conceptual catchment models: The Metropolis algorithm, *J. Hydrol.*, *211*(1–4), 69–85.

Lai, C. T., G. Katul, D. Ellsworth, and R. Oren (2000a), Modelling vegetation-atmosphere CO_2 exchange by a coupled Eulerian-Langrangian approach, *Boundary Layer Meteorol.*, *95*(1), 91–122.

Lai, C. T., G. Katul, R. Oren, D. Ellsworth, and K. Schafer (2000b), Modeling CO_2 and water vapor turbulent flux distributions within a forest canopy, *J. Geophys. Res.*, *105*(D21), 26,333–26,351.

Law, B. E., M. Williams, P. M. Anthoni, D. D. Baldocchi, and M. H. Unsworth (2000), Measuring and modelling seasonal variation of carbon dioxide and water vapour exchange of a *Pinus ponderosa* forest subject to soil water deficit, *Global Change Biol.*, *6*(6), 613–630.

Leuning, R., F. M. Kelliher, D. G. G. Depury, and E. D. Schulze (1995), Leaf nitrogen, photosynthesis, conductance and transpiration: Scaling from leaves to canopies, *Plant Cell Environ.*, *18*(10), 1183–1200.

Lloyd, J., and J. A. Taylor (1994), On the temperature-dependence of soil respiration, *Funct. Ecol.*, *8*(3), 315–323.

Lloyd, J., O. Shibistova, D. Zolotoukhine, O. Kolle, A. Arneth, C. Wirth, J. M. Styles, N. M. Tchebakova, and E. D. Schulze (2002), Seasonal and annual variations in the photosynthetic productivity and carbon balance of a central Siberian pine forest, *Tellus, Ser. B*, *54*(5), 590–610.

Lorenz, E. N. (1956), Empirical orthogonal functions and statistical weather prediction, *Stat. Forecast. Proj. Sci. Rep. 1*, 49 pp., Dep. of Meteorol., Mass. Inst. of Technol., Cambridge.

Mackay, D. S., S. Samanta, R. R. Nemani, and L. E. Band (2003), Multi-objective parameter estimation for simulating canopy transpiration in forested watersheds, *J. Hydrol.*, *277*(3–4), 230–247.

Margulis, S. A., and D. Entekhabi (2003), Variational assimilation of radiometric surface temperature and reference-level micrometeorology into a model of the atmospheric boundary layer and land surface, *Mon. Weather Rev.*, *131*(7), 1272–1288.

Medlyn, B. E., D. Loustau, and S. Delzon (2002), Temperature response of parameters of a biochemically based model of photosynthesis. I. Seasonal changes in mature maritime pine (*Pinus pinaster Ait.*), *Plant Cell Environ.*, *25*, 1155–1165.

Middleton, E. M., J. H. Sullivan, B. D. Bovard, A. J. Deluca, S. S. Chan, and T. A. Cannon (1997), Seasonal variability in foliar characteristics and physiology for boreal forest species at the five Saskatchewan tower sites during the 1994 Boreal Ecosystem-Atmosphere Study, *J. Geophys. Res.*, *102*, 28,831–28,844.

Morecroft, M. D., and J. M. Roberts (1999), Photosynthesis and stomatal conductance of mature canopy Oak (*Quercus robur*) and Sycamore (*Acer pseudoplatanus*) trees throughout the growing season, *Funct. Ecol.*, *13*(3), 332–342.

Noilhan, J., and J. F. Mahfouf (1996), The ISBA land surface parameterisation scheme, *Global Planet. Change*, *13*(1–4), 145–159.

Ogee, J., Y. Brunet, D. Loustau, P. Berbigier, and S. Delzon (2003), MUSICA, a CO_2, water and energy multilayer, multileaf pine forest model: Evaluation from hourly to yearly time scales and sensitivity analysis, *Global Change Biol.*, *9*(5), 697–717.

Pearson, K. (1901), On lines and planes of closest fit to systems of points in space, *Philos. Mag.*, *2*, 559–572.

Pinard, J. D., and J. D. Wilson (2001), First- and second-order closure models for wind in a plant canopy, *J. Appl. Meteorol.*, *40*, 1762–1768.

Poggi, D., A. Porporato, L. Ridolfi, J. D. Albertson, and G. G. Katul (2004), The effect of vegetation density on canopy sub-layer turbulence, *Boundary Layer Meteorol.*, *111*(3), 565–587.

Pyles, R. D., B. C. Weare, and K. T. Paw U (2000), The UCD advanced canopy-atmosphere-soil algorithm: Comparisons with observations from different climate and vegetation regimes, *Q. J. R. Meteorol. Soc.*, *126*(569), 2951–2980.

Reichle, R. H., D. B. McLaughlin, and D. Entekhabi (2001), Variational data assimilation of microwave radiobrightness observations for land surface hydrology applications, *IEEE Trans. Geosci. Remote Sens.*, *39*(8), 1708–1718.

Siqueira, M., C. T. Lai, and G. Katul (2000), Estimating scalar sources, sinks, and fluxes in a forest canopy using Lagrangian, Eulerian, and hybrid inverse models, *J. Geophys. Res.*, *105*, 29,475–29,488.

Styles, J. M., et al. (2002), Soil and canopy CO_2, CO_2–C-13, H_2O and sensible heat flux partitions in a forest canopy inferred from concentration measurements, *Tellus, Ser. B*, *54*(5), 655–676.

Sullivan, J. H., B. D. Bovard, and E. M. Middleton (1997), Variability in leaf-level CO_2 and water fluxes in *Pinus banksiana* and *Picea mariana* in Saskatchewan, *Tree Physiol.*, *17*(8–9), 553–561.

Tracy, C. R., F. H. Vanberkum, J. S. Tsuji, R. D. Stevenson, J. A. Nelson, B. M. Barnes, and R. B. Huey (1984), Errors resulting from linear-approximations in energy-balance equations, *J. Therm. Biol.*, *9*(4), 261–264.

von Storch, H. (1999), Spatial patterns: EOFs and CCA, in *Analysis of Climate Variability: Applications of Statistical Techniques*, edited by H. von Storch and A. Navarra, pp. 227–257, Springer, New York.

von Storch, H., and F. W. Zwiers (1999), *Statistical Analysis in Climate Research*, 494 pp., Cambridge Univ. Press, New York.

Wang, Y. P., R. Leuning, H. A. Cleugh, and P. A. Coppin (2001), Parameter estimation in surface exchange models using nonlinear inversion: How many parameters can we estimate and which measurements are most useful?, *Global Change Biol.*, *7*(5), 495–510.

Williams, M., E. B. Rastetter, D. N. Fernandes, M. L. Goulden, S. C. Wofsy, G. R. Shaver, J. M. Melillo, J. W. Munger, S. M. Fan, and K. J. Nadelhoffer (1996), Modelling the soil-plant-atmosphere continuum in a Quercus-Acer stand at Harvard forest: The regulation of stomatal conductance by light, nitrogen and soil/plant hydraulic properties, *Plant Cell Environ.*, *19*(8), 911–927.

Wilson, K. B., D. D. Baldocchi, and P. J. Hanson (2000a), Quantifying stomatal and non-stomatal limitations to carbon assimilation resulting from leaf aging and drought in mature deciduous tree species, *Tree Physiol.*, *20*(12), 787–797.

Wilson, K. B., D. D. Baldocchi, and P. J. Hanson (2000b), Spatial and seasonal variability of photosynthetic parameters and their relationship to leaf nitrogen in a deciduous forest, *Tree Physiol.*, *20*(9), 565–578.

Wilson, K. B., D. D. Baldocchi, and P. J. Hanson (2001), Leaf age affects the seasonal pattern of photosynthetic capacity and net ecosystem exchange of carbon in a deciduous forest, *Plant Cell Environ.*, *24*(6), 571–583.

Wullschleger, S. D. (1993), Biochemical limitations to carbon assimilation in C_3 plants: A retrospective analysis of the a/Ci curves from 109 species, *J. Exp. Bot.*, *44*(262), 907–920.

Xu, L., and D. Baldocchi (2003), Seasonal trends in photosynthetic parameters and stomatal conductance of blue oak (*Quercus douglasii*) under prolonged summer drought and high temperature, *Tree Physiol.*, *23*, 865–877.

J. D. Albertson and D. T. Drewry, Department of Civil and Environmental Engineering, 217 Hudson Hall, Box 90827 Duke University, Durham, NC 27708-0287, USA. (darren.drewry@duke.edu)